Eur. Phys. J. B **30**, 319–329 (2002)
DOI: 10.1140/epjb/e2002-00385-4

THE EUROPEAN PHYSICAL JOURNAL B

Broad-band dielectric spectroscopy of $Ba_2NaNb_5O_{15}$ single crystal

E. Buixaderas[a], V. Porokhonskyy, A. Paskhin, M. Savinov, and J. Petzelt

Institute of Physics, ASCR, Na Slovance 2, 182 21 Prague 8, Czech Republic

Received 24 August 2002
Published online 19 December 2002 –

Abstract. Barium sodium niobate (BNN) single crystals are studied by IR spectroscopy, time-domain THz transmission spectroscopy, HF coaxial wave-guide technique and LF dielectric spectroscopy to cover the frequency range 10^2–10^{14} Hz in a wide temperature interval. The dielectric response parallel and perpendicular to the polar c-axis is discussed. The ferroelectric transition at $T_c = 830$ K is driven by a relaxational soft mode coupled with another central-mode type relaxation which both gradually disappear on cooling in the ferroelectric phase. Below T_i the parameters of the expected IR active amplitudon were estimated. The low-temperature permittivity increase on cooling for the $\boldsymbol{E}\perp\boldsymbol{c}$ field direction has been explained by an incipient proper ferroelectric-ferroelastic transition driven by an IR and Raman active B_2-symmetry soft mode.

PACS. 63.20.-e Phonons in crystal lattices – 64.70.Rh Commensurate-incommensurate transitions – 77.80.Bh Phase transitions and Curie point – 77.84.-s Dielectric, piezoelectric, ferroelectric, and antiferroelectric materials

1 Introduction

$Ba_2NaNb_5O_{15}$ (BNN) belongs to the family of tungsten-bronze-type ferroelectrics. It has been widely studied owing to its promising applications in nonlinear optics and electro-optics [1] and to its rich sequence of phase transitions. At high temperatures it has a tetragonal symmetry (space group P4/mbm-D^5_{4h}, $Z = 2$), then at $T_c = 830$ K it undergoes a proper ferroelectric phase transition (PT) to another tetragonal phase I4bm-C^2_{4v} with a spontaneous polarization parallel to the c-axis [2]. At $T_i \cong 573$ K BNN passes through an incommensurate (IC)-ferroelastic PT [3] and the resulting structure, with averaged orthorhombic symmetry, has a modulation vector $\boldsymbol{q} = (1 + \delta)/4(\boldsymbol{a}^*_t + \boldsymbol{b}^*_t) + 1/2\boldsymbol{c}^*$ (referred to the tetragonal axes). The space group corresponding to $\delta = 0$ is Bbm2-C^{16}_{2v} [4]. The unit cell is doubled along the c-axis and the commensurate modulation gives rise to a doubling of the lattice parameter along the tetragonal $a_t b_t$-diagonal (orthorhombic a-axis) [5]. On further cooling (near $T \cong 543$ K), domains with a new modulation coexist and at $T_L \cong 503$ K an almost lock-in transition to a quasi-commensurate state occurs [3], with a residual modulation ($\delta \sim 0.01$) along the orthorhombic a-axis. This δ-value remains constant down to room temperature (RT) at least [4]. At $T_0 = 110$ K another PT appears. Some authors reported that the symmetry below T_0 remains orthorhombic or quasi-tetragonal and that another doubling of the unit cell occurs along the orthorhombic b-axis [6–8], but it was also reported that the appearance of the PT is strongly sample-dependent and that in some cases the tetragonal 4mm point symmetry was recovered [9–11].

Near the ferroelectric PT, an overdamped soft mode plus a central mode of almost constant frequency (both of A_1 symmetry) were revealed in Raman scattering [12]. Concerning the ferroelastic-IC transition, a Raman mode of symmetry B_2 was found below 573 K to soften on cooling [13,14] together with another central mode. Neutron scattering revealed an underdamped mode near the lock-in wave vector [4], which softens approaching T_i and becomes overdamped below T_i. The dielectric behaviour of BNN was reported in [11,15,16].

Concerning IR measurements, we extended the RT IR measurements on powders [17] and single crystals [18] to the broad temperature range in two different polarizations in reference [19]. In the present paper we have completed the IR data by the time-domain THz, high frequency (HF), low frequency (LF) dielectric measurements on the same samples and performed a new fit to the combined IR and THz spectra to shed light on the origin of the low-frequency dielectric behaviour and dynamic origin of all the PTs.

2 Experimental

A BNN single crystal was grown by the Czochralski method and cut in two plates of [001] and [100] orientations to enable measurements in the $\boldsymbol{E} \parallel \boldsymbol{c}$ and $\boldsymbol{E}\perp\boldsymbol{c}$

[a] e-mail: buixader@fzu.cz

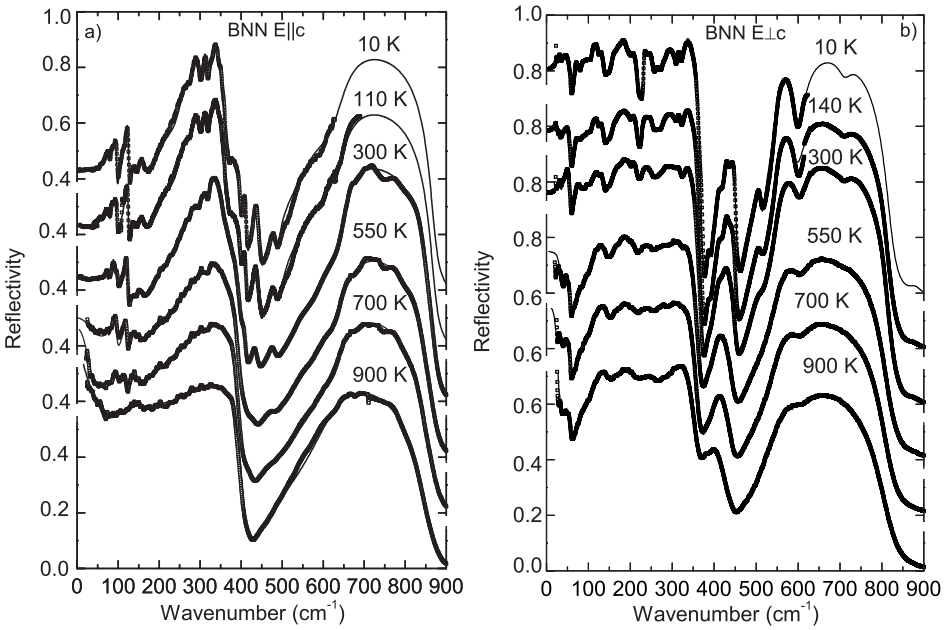

Fig. 1. IR and THz reflectivity spectra together with their fits (thin solid lines) at several temperatures for (a) $\boldsymbol{E} \parallel \boldsymbol{c}$ and (b) $\boldsymbol{E} \perp \boldsymbol{c}$ polarizations.

polarizations. The samples were studied by means of far-IR reflectivity, time-domain THz transmission spectroscopy (90 GHz–2.5 THz), HF coaxial technique (1 MHz–1.8 GHz), and LF dielectric spectroscopy (100 Hz–1 MHz).

IR reflectivity measurements were performed using a Fourier spectrometer Bruker IFS 113v equipped with two RT DTGS pyroelectric detectors as well as He-cooled (1.5 K) Si bolometer. Spectra were measured in the range 20–4000 cm^{-1}. For low temperature measurements (from 300 to 10 K) we used a continuous-flow Oxford CF 104 cryostat with the sample mounted on a vacuum cold finger. For high temperatures (300–900 K) a custom-made oven was used. To polarize the light we used a metal-mesh polarizer deposited on a thin polyethylene foil.

For dielectric measurements in the HF range two cylindrical samples were cut (of heights h and diameters d: $h_1 = 0.62$ mm, $d_1 = 0.78$ mm and $h_2 = 2.002$ mm, $d_2 = 0.68$ mm, with the polar axis parallel and perpendicular, respectively, to the axis of the cylinder). A computer controlled HF dielectric spectrometer equipped with HP 4291B impedance analyzer, a NOVOCONTROL BDS 2100 coaxial sample cell and a SIGMA SYSTEM M18 temperature chamber (operation range 100–570 K) were used. The impedance of the sample with Au electrodes sputtered on the bases of the cylinders was recorded on cooling at a rate 1 K/min. The dielectric parameters were calculated taking into account the electromagnetic field distribution in the sample [20,21].

THz transmission measurements were done on two thin polished plane-parallel samples ($4.7 \times 7.8 \times 0.33$ mm^3 and $4.4 \times 7.8 \times 0.33\,\mathrm{mm}^3$) in the temperature range 15–300 K. A custom-made time-domain THz transmission spectrometer was used to obtain the complex dielectric response from 3 to 80 cm^{-1} with a resolution of 0.5 cm^{-1}. This spectrometer uses a femtosecond Ti: sapphire laser and a biased large-aperture antenna from a low-temperature grown GaAs as THz emitter, and an electro-optic sampling detection technique [22]. An Optistat CF cryostat with mylar windows (with thickness of 25 and 50 μm for the inner and outside windows, respectively) was used for measurements down to 10 K.

For LF dielectric measurements using the Hewlett-Packard impedance analyser 4192A LF, silver paste electrodes were added onto the faces of the above cited plates. The samples were heated and cooled in the temperature range of 13–930 K at a velocity rate of 3 K/min under a measurement field of 40 V/cm.

3 Results and evaluation

3.1 IR measurements

The experimental reflectivity spectra published in [19] were renormalized and refitted using the new THz and HF values with the generalized oscillator model of the dielectric function due to the presence of broad and asymmetric reflection bands [23]

$$\hat{\varepsilon}(\omega) = \varepsilon'(\omega) + \mathrm{i}\varepsilon'' = \varepsilon_\infty \prod_{i=1}^{n} \frac{\omega_{LOi}^2 - \omega^2 + \mathrm{i}\omega\gamma_{LOi}}{\omega_{TOi}^2 - \omega^2 + \mathrm{i}\omega\gamma_{TOi}}, \quad (1)$$

where ε_∞ is the permittivity at frequencies much higher than all polar phonon oscillator eigenfrequencies, ω_{TOi} and ω_{LOi} are the eigenfrequencies of the transverse and longitudinal ith phonon mode and γ_{TOi} and γ_{LOi} their respective damping constants. In Figure 1 we present the renormalized spectra including the THz reflectivity points together with the fit for both polarizations at selected temperatures.

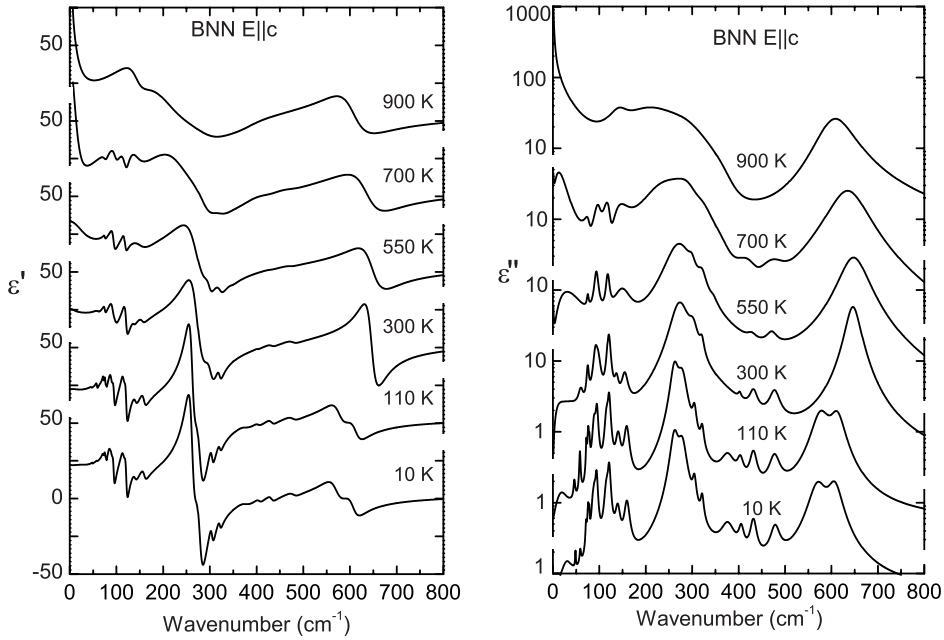

Fig. 2. Temperature dependence of the permittivity and losses obtained from the fit of the IR reflectivity for a BNN single crystal for the $\boldsymbol{E} \parallel \boldsymbol{c}$ polarization.

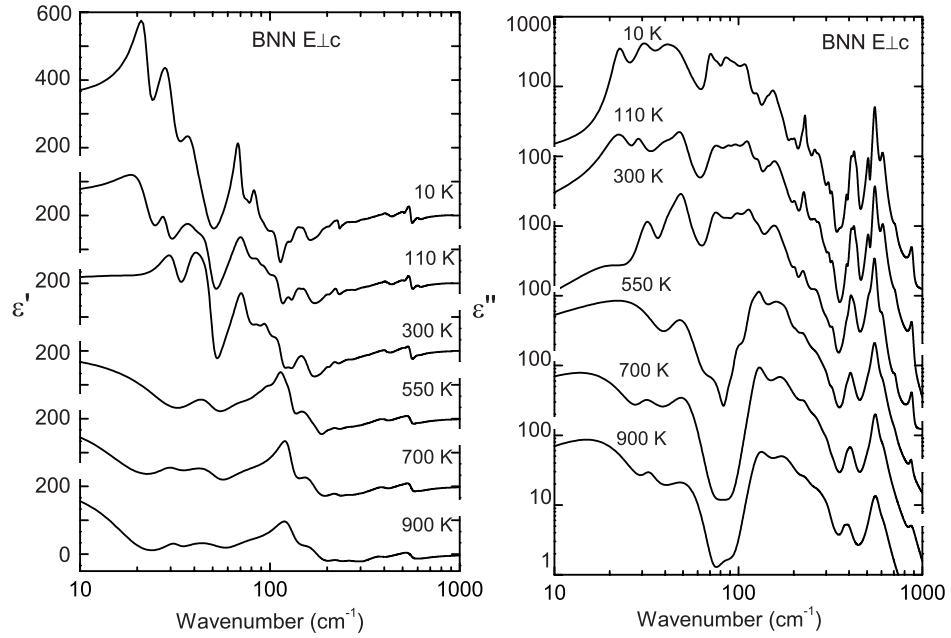

Fig. 3. Temperature dependence of the permittivity and losses obtained from the fit of the IR reflectivity for a BNN single crystal for the $\boldsymbol{E} \perp \boldsymbol{c}$ polarization.

In Figure 2 the $\boldsymbol{E} \parallel \boldsymbol{c}$ polarized dielectric spectra calculated from the fit are presented. One sees that the permittivity due to the phonon contribution is low ($\varepsilon' \sim 25$) and that at high temperatures another excitation is present below the phonon frequencies which increases the low-frequency ε' and ε'' values. In the high temperature paraelectric phase five highly damped modes plus two low-frequency overdamped excitations were detected. At low temperatures new modes appear, altogether 23 at the lowest temperature. In Figure 3 the $\boldsymbol{E} \perp \boldsymbol{c}$ polarized spectra are depicted. The most interesting feature is the increase of the low-frequency permittivity on cooling (from ∼150 at 900 K to ∼380 at 10 K). More modes were detected in this polarization (14 in the paraelectric phase and 34 in the lowest one). The fitted modes in both polarizations at 900 K (paraelectric phase), 300 K (ferroelastic-IC

Table 1. Parameters of the IR phonons for both polarizations at selected temperatures.

$E \perp c$									$E \parallel c$								
10 K			300 K			900 K			10 K			300 K			900 K		
ω_T	γ_T	$\Delta\varepsilon$	ω_T	γ_T	$\Delta\varepsilon$	ω_T	γ_T	$\Delta\varepsilon$	ω_T	γ_T	$\Delta\varepsilon$	ω_T	γ_T	$\Delta\varepsilon$	ω_T	γ_T	$\Delta\varepsilon$
18.2		20	23.0		42	21.1		100	22.2	20.4	0.5	17.7	35.6	2.1	0.54		2421
22.5	3.8	51.9	32.1	7.5	32.0	21.1	24.5	99.5	47.8	8.4	0.1	46.6	15.0	0.4	14.1	124.8	70.5
30.3	7.7	86.4	-			32.4	7.23	6.5	59.9	4.2	0.06	60.6	11.3	0.2	-		
39.7	11.9	64.7	39.6	12.4	21.3	-			71.4	2.7	0.1				-		
44.0	14.1	47.6	49.4	9.0	34.7	57.5	36.1	11.6	76.0	0.3	0.3	75.1	5.3	0.4	-		
69.4	7.1	18.5	72.9	13.6	22.4	-			78.3	3.8	0.06	-			-		
77.7	7.7	4.6	-			-			85.9	1.4	0.2	-			-		
83.5	10.4	13.3	88.5	11.8	2.3	86.8	74.0	5.8	89.4	5.3	0.8	90.3	9.2	1.1	-		
95.4	15.0	0.8	95.7	15.3	5.4	-			94.3	5.4	0.7	93.4	11.8	1.1	-		
111.6	13.5	10.8	115.2	15.7	9.2	-			109.7	11.9	0.1	-			-		
128.3	12.0	2.0	130.3	16.4	3.8	128.7	36.1	32.2	122.3	6.2	1.5	120.6	7.8	1.3	-		
146.0	10.3	1.0	-			-			137.2	14.5	0.8	141.6	20.2	0.3	145.0	49.7	151.4
155.1	26.2	12.3	161.0	36.2	22.5	173.1	66.3	26.6	156.0	19.6	0.7	157.4	27.3	1.2	-		
179.2	27.2	1.8	180.9	32.1	3.3	-			213.8	44.7	0.4	214.4	50.6	0.4	207.3	158.1	20.1
194.1	16.6	0.8	204.1	12.3	0.4	-			257.2	33.9	5.6	261.4	45.0	6.6	-		
201.5	13.2	0.6	-			-			283.6	21.4	0.4	283.0	24.0	0.3	293.3	121.6	1.6
222.2	11.6	0.3	224.7	23.2	1.6	227.5	39.2	2.1	306.9	14.6	0.5	304.5	18.1	0.6	-		
230.7	7.7	0.6	-			-			323.9	23.2	0.8	322.5	25.0	1.1	-		
243.4	24.9	0.9	-			-			382.0	31.6	0.2	379.0	53.8	0.3	377.2	91.2	0.03
259.9	16.5	0.4	-			-			408.4	8.9	0.03	407.5	27.7	0.1	-		
274.2	26.3	0.6	271.4	43.0	1.2	270.4	54.4	1.6	434.1	15.3	0.1	432.5	26.0	0.2	-		
291.8	29.9	0.2	-			-			483.2	13.6	0.04	481.9	32.1	0.1	-		
314.2	13.8	0.1	314.0	40.9	0.4	307.8	47.7	0.4	560.5	86.0	0.4	619.8	67.5	1.3	-		
320.4	26.6	0.4	322.5	26.8	0.2	-			664.0	60.8	2.0	653.2	33.1	1.7	606.7	105	3.2
358.0	45.2	0.1	-			-											
426.4	16.1	0.3	426.1	41.5	0.7	-											
439.2	20.2	0.2	-			-											
511.1	16.6	0.2	511.9	32.0	0.3	-											
550.9	24.8	2.3	550.5	33.3	2.3	557.0	78.0	3.0									
608.0	39.1	0.6	602.5	45.5	0.3	601.9	77.9	0.4									
712.3	36.9	0.01	712.3	36.1	0.01	-											
880.9	40.2	0.01	880.9	40.2	0.01	874.3	98.9	0.02									

phase) and at the lowest measured temperature 10 K are presented in Table 1. For each temperature the transverse optical phonon frequency ω_T, its damping γ_T and the dielectric strength $\Delta\varepsilon$ are listed.

3.2 THz, microwave and dielectric measurements

In Figures 4 and 5 we present the permittivity and loss spectra for selected temperatures in the spectral range 10^5 to 10^{14} Hz in both polarizations including the IR fit. In the $\boldsymbol{E} \parallel \boldsymbol{c}$ polarization (Fig. 4) the THz data revealed that there is no dispersion below but near the phonon region in the temperature range 300–10 K. The agreement between FIR and THz data is very good. The HF data measured between 100–550 K showed anomalous oscillations, which are attributed to piezoelectric resonances in the sample. On lowering the frequency, they raise gradually the value of the clamped permittivity up to the value of the stress free permittivity below 1 MHz. The results of the LF dielectric measurements revealed a strong increase in ε' due to the ferroelectric transition at 830 K. Two overdamped modes (relaxators) were used to account for the difference between the IR-THz data and the HF-LF values following reference [12], the lowest frequency one corresponding to a central mode and the other to the ferroelectric soft mode. At highest temperatures (700 K, 550 K) two corresponding peaks are seen in the loss spectra in the range 10^9–10^{11} Hz. At 900 K the central mode is so intense that just one peak is seen around 10^{10} Hz. The LF values of the permittivity are in agreement with those published [15]. We have to mention that the LF measurements show weak anomalies in ε_c'' between 200 and 400 K probably related to the presence of discommensurations. No anomaly in ε_c' is found near T_0.

For the $\boldsymbol{E} \perp \boldsymbol{c}$ polarization (Fig. 5), the THz, HF and LF values agree quite well although the LF permittivity is slightly higher than the HF one. The difference is due to geometrical approximations, which differ for both experimental approaches, and lies within the accuracy limits of both techniques. The increase in ε' below RT on cooling is detected by all the techniques. No additional dispersion is present below the phonons, but an extra central mode was added to obtain the LF values at high temperatures where the HF data are missing. This central mode is weaker than the previous one seen in the loss spectra. The LF data show two small anomalies in the loss spectra in the range 500–600 K connected apparently with the discommensurations.

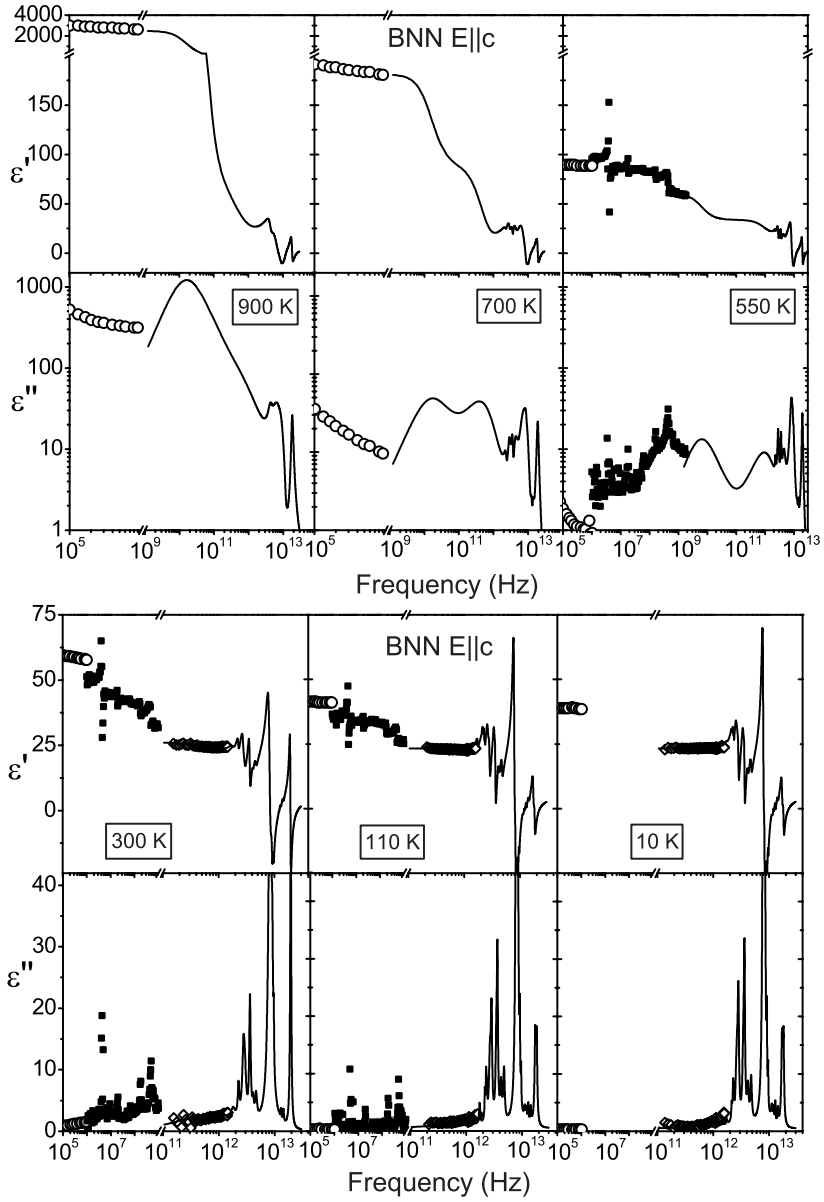

Fig. 4. Permittivity and loss spectra of BNN at several temperatures in the frequency range of 10^5–10^{14} Hz for the $\boldsymbol{E} \parallel \boldsymbol{c}$ polarization. THz data are represented by diamonds, HF data by black squares and LF dielectric data by circles. The IR fit is shown by a solid line. Note the log scales and piezoelectric resonances in the HF spectral range.

4 Discussion

4.1 IR spectra and symmetry considerations

The factor-group analyses for the RT phase and for the tetragonal phases were published in references [17,24]. In Table 2 the symmetry classification of the phonon modes in different phases is shown. In the paraelectric phase 138 modes exist at the Γ-point of the Brillouin zone, corresponding to the 2 formula units in the unit cell. Out of them, one A_{2u} mode and one E_u doublet are the acoustic ones. 8 A_{2u} and 25 E_u optic modes are IR active in the $\boldsymbol{E} \parallel \boldsymbol{c}$ and $\boldsymbol{E} \perp \boldsymbol{c}$ polarizations, respectively. The mode dampings in this phase ($T > 830$ K) are very high so that the number of IR modes detected in our IR experiment is lower. Correlation into the ferroelectric phase following the table gives the number of active modes below T_c. The order-parameter representation should have symmetry A_{2u}, giving rise to the spontaneous polarization parallel to the c-axis. Hence, the soft mode responsible for such a transition should be seen in the $\boldsymbol{E} \parallel \boldsymbol{c}$ polarized spectra (A_{2u} and A_1 symmetries above and below T_c, respectively).

At the IC-ferroelastic PT a quadrupling of the primitive unit cell (doubling simultaneously along the a and c axes) occurs, resulting in $Z_p = 8$, (the index p refers to the primitive cell, which is half the conventional crystallographic cell). The factor-group analysis taking the

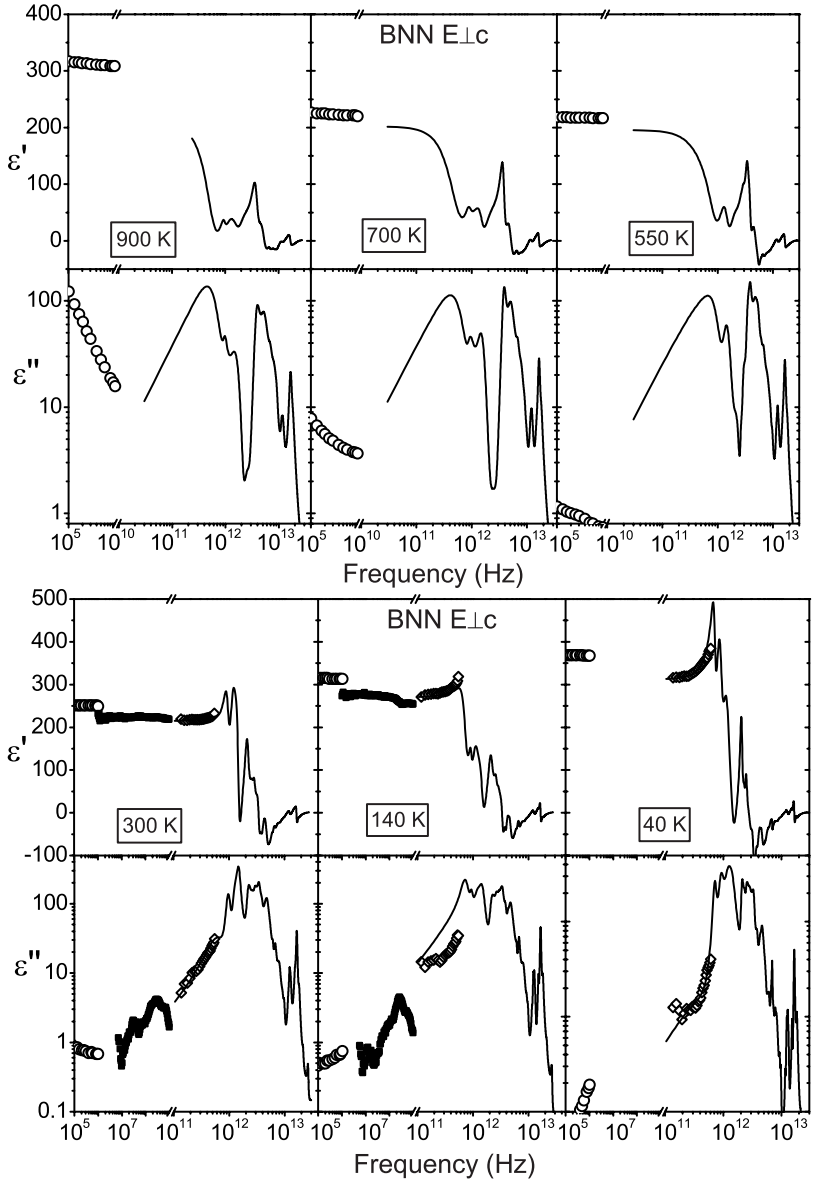

Fig. 5. Permittivity and loss spectra of BNN at several temperatures in the frequency range of 10^5–10^{14} Hz for the $\boldsymbol{E}\perp\boldsymbol{c}$ polarization. THz data are represented by diamonds, HF data by black squares and LF dielectric data by circles. The IR fit is shown by a solid line. Note the log scales.

structural results by Jamieson *et al.* [2], which neglects both doublings, gives the result in the third column of Table 2, in total 174 modes. In this analysis partial occupancy of Ba and O atoms was taken into account, which gives a higher number of effective atoms (vibrational degrees of freedom) in the unit cell. This orthorhombic cell has the following axes with respect to the tetragonal ones: $\boldsymbol{a} = (\boldsymbol{a}_t - \boldsymbol{b}_t)$, $\boldsymbol{b} = (\boldsymbol{a}_t + \boldsymbol{b}_t)$, $\boldsymbol{c} = \boldsymbol{c}_t$. However to make a more rigorous estimation of the number of modes at RT one should take into account both doublings. In this case the space group is Bbm2-C_{2v}^{16} [4]. As no new crystallographic data are available we took the positions and site symmetries of the atoms in the symmetry group Ccm2-C_{2v}^{11} [2] and transformed them into the new group Bbm2-C_{2v}^{16}. In this case the new orthorhombic cell is related to the tetragonal one by $\boldsymbol{a} = 2(\boldsymbol{a}_t - \boldsymbol{b}_t)$, $\boldsymbol{b} = (\boldsymbol{a}_t + \boldsymbol{b}_t)$, $\boldsymbol{c} = 2\boldsymbol{c}_t$. The Wyckoff positions for all the atoms are given in Table 2. With these occupied sites the factor-group analysis gives the results of the fourth column in Table 2. Again, owing to the partial occupancy of some sites, there is a disorder in the crystal and the number of effective modes is higher.

Different attempts were made to explain the origin of the PT at T_i. The simplest case was considered by Yamada *et al.* [15] in which the transition is due to an elastic instability, driven by a one-dimensional order parameter (the strain component e_6) of B_2 symmetry. However, this attempt did not consider both doublings of the unit cell. As shown by Toledano [25] the PT taking into account the doubling along the c-axis – this fact requires the space

Table 2. Factor-group analysis of BNN showing the correlation among different phases. The results for the paraelectric and ferroelectric phases are taken from reference [24].

Phase	Paraelectric	Ferroelectric	Ferroelastic I	Ferroelastic II
Space group	P4/mbm (D^5_{4h})	P4bm (C^2_{4v})	Cmm2 (C^{11}_{2v})	Bbm2 (C^{16}_{2v})
	Z = 2	Z = 2 P_s||(001)	$Z_p = 2$	$Z_p = 8$ ($\delta = 0$)
Active modes	10 $A_{1g}(a_t^2,\ b_t^2,\ c^2)$	19 A_1(c; $a_t^2,\ b_t^2,\ c^2$)		
	9 A_{2u}(c)			
			46 A_1(c; a^2, b^2, c^2)	183 A_1(c; $a^2,\ b^2,\ c^2$)
	8 $B_{1u}(-)$	18 $B_2(a_tb_t)$		
	10 $B_{2g}(a_tb_t)$			
	5 $A_{1u}(-)$	15 $A_2(-)$		
	10 $A_{2g}(-)$			
			39 $A_2(ab)$	163 $A_2(ab)$
	10 $B_{1g}(a_t^2,\ b_t^2)$	14 $B_1(a_t^2,\ b_t^2)$		
	4 $B_{2u}(-)$			
	10 $E_g(a_tc,\ b_tc)$	36 E(a_t, b_t; $a_tc,\ b_tc$)	46 B_1(a, ac)	165 B_1(a, ac)
	26 $E_u(a_t,\ b_t)$		43 B_2(b, bc)	185 B_2(b, bc)
Total	138 modes	138 modes	174 modes	696 modes
Atom sites			Na: 1($4c$)	Na: 2($4a$)+1($8c$)
			Ba: 1($4d$)+1($8f$)	Ba: 4($4b$)+4($8c$)
			Nb: 1($2a$)+1($2b$)+2($8f$)	Nb: 4($4b$)+8($8c$)
			O: 3($4d$)+1($4e$)+8($8f$)	O: 12($4b$)+34($8c$)

group of the low-temperature phase to be $Ccm2_1$-C^{12}_{2v} – would involve a two dimensional order parameter of E symmetry (in the Z point of the Brillouin Zone). However, his approach neglected the doubling along the diagonal. The last attempt by Schneck *et al.* [4], including both doublings and the incommensuration, lead to a four-dimensional order parameter which corresponds to a lattice instability at the lock-in wave vector $(1/4, 1/4, 1/2)_t$ revealed by neutron scattering. This order parameter is linearly coupled with the strain only below the PT leading to improper ferroelasticity, which explains the absence of a soft Raman mode above this PT.

4.2 Piezoelectric resonances

Owing to the mm2 symmetry of the IC-ferroelastic phase at RT, piezoelectric resonances are allowed in all three components of the dielectric response. The five piezoelectric moduli and the elastic stiffness constants were already measured [26], and the values are listed in Table 3. The integral contribution of the piezoelectricity to the stress free (low-frequency) permittivity can be calculated by the formula [27],

$$\Delta\varepsilon_{ij}^{\text{piez}} = \varepsilon_{ij}^{\text{free}} - \varepsilon_{ij}^{\text{clamped}} = \sum_{k,l} d_{ik}\, d_{il}\, c_{kl}/\varepsilon_0, \qquad (2)$$

where $\varepsilon_{ij}^{\text{free}}$ and $\varepsilon_{ij}^{\text{clamped}}$ stand for the values of the stress free and clamped (above all the piezoelectric resonances) permittivities, d_{ik} are the piezoelectric moduli, c_{kl} are the stiffness constants, and ε_0 the permittivity of vacuum ($8.85\ 10^{-12}$ F/m). This contribution is independent of the sample geometry. For BNN, taking the values from Table 3 we obtained the results: $\Delta\varepsilon_{33}^{\text{piez}} = 18.64$ for the $\boldsymbol{E} \parallel \boldsymbol{c}$ geometry and $\Delta\varepsilon_{11}^{\text{piez}} = 13.16$, $\Delta\varepsilon_{22}^{\text{piez}} = 19.86$ for the $\boldsymbol{E}\perp\boldsymbol{c}$ geometry. The piezoelectric contribution matches very well the increase observed in the HF data at RT for $\boldsymbol{E} \parallel \boldsymbol{c}$, where the total increase is $\Delta\varepsilon_c^{\text{piez}} = \varepsilon_c^{\text{free}}$ (1MHz)-$\varepsilon_c^{\text{clamped}}$ (1.8 GHz)=50–32=18.

Table 3. Elastic stiffness and piezoelectric moduli for BNN measured in reference [26].

Piezoelectric moduli (C/N)		Elastic stiffness constants (N/m^2)	
d_{15}	4.2×10^{-11}	c_{11}^{E}	2.39×10^{11}
d_{24}	5.2×10^{-11}	c_{12}^{E}	1.04×10^{11}
d_{31}	-0.7×10^{-11}	c_{13}^{E}	0.50×10^{11}
d_{32}	-0.6×10^{-11}	c_{22}^{E}	2.47×10^{11}
d_{33}	3.7×10^{-11}	c_{23}^{E}	0.52×10^{11}
		c_{33}^{E}	1.35×10^{11}
		c_{44}^{E}	0.65×10^{11}
		c_{55}^{E}	0.66×10^{11}
		c_{66}^{E}	0.76×10^{11}

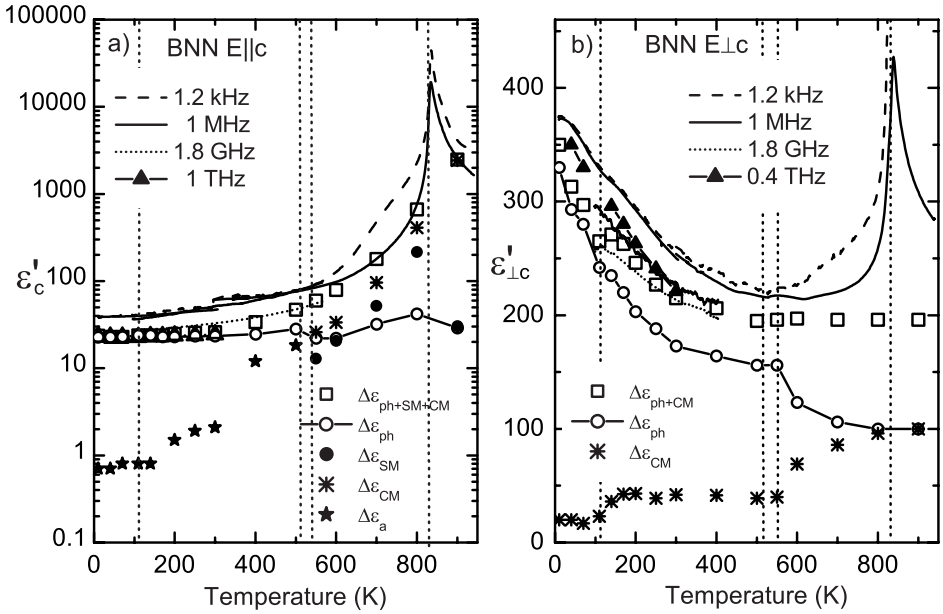

Fig. 6. Dielectric contribution of the phonons and the extra central-mode type excitation in a BNN crystal together with experimental values of the permittivity at various frequencies (a) $\boldsymbol{E} \parallel \boldsymbol{c}$ polarization; (b) $\boldsymbol{E} \perp \boldsymbol{c}$ polarization. Note the log scale in (a).

A rough estimate of the fundamental resonance frequencies –for plates of about 0.6 mm thickness– situates them in the MHz range, with slightly lower frequencies for transverse (shear) modes than for the longitudinal ones. Even if our samples have different geometry we see the resonances of the longitudinal modes in the $\boldsymbol{E} \parallel \boldsymbol{c}$ HF spectra, which is in agreement with the predictions. However, it is difficult to estimate if some resonances are present in the $\boldsymbol{E} \perp \boldsymbol{c}$ spectra. In this case the piezoelectric contribution is very small, about 8% of the clamped-permittivity value ($\varepsilon' \sim 220$), so that the resonances must be tiny. Moreover the presence of ferroelectric and ferroelastic domain walls and in addition of the discommensurations may attenuate the piezoelectric resonances, which could explain their near absence in our dielectric spectra. Some traces of them are seen in the HF loss spectra (see Fig. 5).

4.3 Dielectric behaviour

The dielectric behaviour of BNN is discussed using Figure 6, where the dielectric permittivity versus temperature is depicted for several fixed frequencies in both polarizations.

Figure 6a shows the permittivity values for the $\boldsymbol{E} \parallel \boldsymbol{c}$ polarization at several frequencies together with the temperature dependence of the total phonon contribution ($\Delta\varepsilon_{\rm ph}$), the contribution of the overdamped ferroelectric soft mode ($\Delta\varepsilon_{\rm SM}$) and the excitation of central-mode type ($\Delta\varepsilon_{\rm CM}$), and the summed up contribution of phonons, soft mode and central mode, $\Delta\varepsilon_{\rm ph+SM+CM}$, in order to compare it with the directly measured values. The phonon contribution (A_1 symmetry in the ferro-phase) to ε_c is about 25 at low temperatures but at $T > 500$ K the damping is so high that the exact evaluation of the mode frequencies is not unambiguous. According to the Raman experiment [12], the Rayleigh wing is broad and temperature dependent. This was interpreted as due to an overdamped soft mode plus a central mode of almost temperature independent frequency. The huge anomaly at the ferroelectric PT seems to be caused by this overdamped soft mode coupled with the central mode. Following this result, two extra modes were added to our IR fit (the ferroelectric soft mode is denoted by stars and the central mode by crosses in Fig. 6a) which accounts practically for the whole dielectric anomaly. The contribution to the permittivity of these two modes can be seen in Figure 6a. On cooling, the still overdamped soft mode hardens and loses its strength disappearing from the spectra below 550 K, as well as the central mode. This is a typical behaviour of a critical relaxation and therefore the ferroelectric PT can be considered as almost order-disorder type. Above $T_{\rm i}$, the goal of the fit was to obtain the LF permittivity values in the para- and ferroelectric phases, however we have to mention that piezoelectric resonances and also contribution from ferroelectric domain walls could be present in the MHz range (see Fig. 4). Therefore the dielectric-strength value of both overdamped modes is not quantitatively accurate.

Below $T_{\rm i}$ a new polar soft mode (the uniform long-wavelength amplitudon) is expected to become active in $\boldsymbol{E} \parallel \boldsymbol{c}$ polarization. This mode is related to the existence of the IC modulation and was already discovered above $T_{\rm i}$ by neutron scattering [4]. Its IR frequency just below $T_{\rm i}$ should be close to zero and should increase on cooling. In order to obtain the HF ε'-values we added a new excitation from 500 K to RT. Below RT it becomes very weak but it helps to fit better the THz permittivity and reflectivity. This new excitation seems to correspond to the

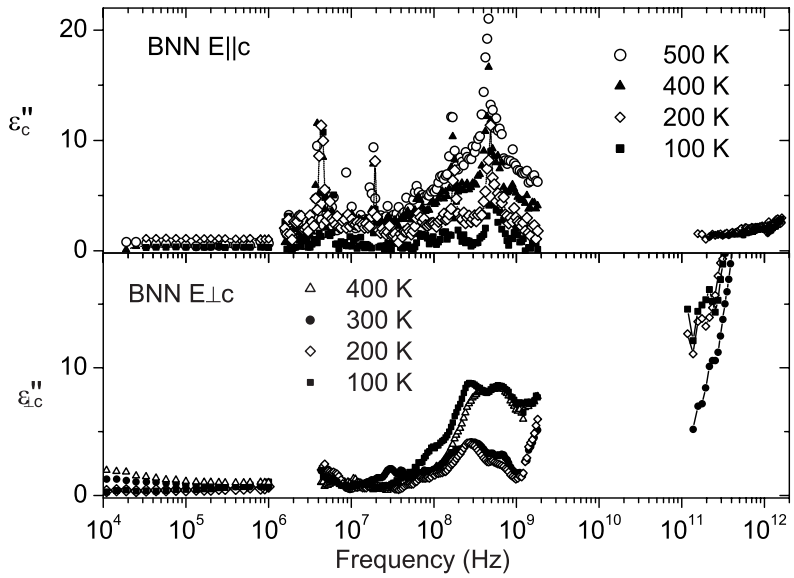

Fig. 7. Loss spectra of BNN measured in the kHz to THz range at temperatures below T_i. Note the piezoelectric resonances in the HF spectral range for the $\boldsymbol{E} \parallel \boldsymbol{c}$ polarization.

amplitudon (denoted by stars in Fig. 6a). Its frequency hardens on cooling and stabilizes below RT and its dielectric strength therefore decreases from ∼10 to ∼1. We have to mention that in the 300–550 K range, owing to the lack of THz data and the presence of the piezoelectric resonances and domains, it was difficult to estimate exactly the parameters of the amplitudon.

Therefore, the results of our fit reveal that the ferroelectric PT is caused by an overdamped soft mode coupled with a central mode excitation. These excitations are anharmonic and the soft mode plays the role of a critical relaxation showing a critical slowing down. On further cooling the soft mode becomes weak and finally disappears. The ferroelastic-IC PT manifests itself by the amplitudon, which becomes active in the IR spectra below T_i.

In Figure 6b the permittivity *versus* temperature behaviour for the $\boldsymbol{E}\perp\boldsymbol{c}$ polarization is presented for similar frequencies as above. Here as well, the IR phonons (E-symmetry modes in the ferro-phase) are not able to account completely for the LF permittivity (see Fig. 4). The difference at high temperatures was accounted for by an overdamped mode whose strength decreases on cooling while the phonon contribution increases. The temperature behaviour of this mode differs, however, from that found from Brillouin [28] and neutron scattering [4] where a maximum of the intensity/strength is seen near T_i. Neglecting the leakage of the strong permittivity anomaly near the ferroelectric PT from the $\boldsymbol{E} \parallel \boldsymbol{c}$ polarization, the most interesting effect seen is the increase of the permittivity on cooling. This increase remains present in the THz range. Therefore it is clear that it has a phononic origin. Below the THz range, no appreciable dielectric dispersion remains below RT. A B_2 soft phonon mode (symmetry valid for the ferroelastic phase) was actually revealed in the Raman spectra [13,14] and should be responsible for it. Using our THz data, this mode can be localized between 20 and 30 cm^{-1} (B_2 modes are both Raman and IR active, see Tab. 2). Following the tables by Janovec *et al.* [29] it can be seen that a Landau-type PT is approached from the orthorhombic mm2 phase with an order parameter of B_2 symmetry to result in a monoclinic m phase. This PT should be both proper ferroelectric and ferroelastic with the appearance of a P_s component along the b-axis and shear deformation u_{yz}. The detected soft mode together with the increase in the permittivity is a precursor of this new hypothetical ferroelectric PT below 0 K.

Interesting data were found in both loss spectra. The values measured at lower frequencies were higher than those from the IR extrapolation. It appears that the ε'' values are higher due to the disorder causing a background absorption of non phononic origin. In Figure 7 the connection of all the measured spectral ranges is depicted for both polarizations. One sees that BNN shows almost constant losses in $\boldsymbol{E} \parallel \boldsymbol{c}$ polarization from MHz to THz below 500 K (except for the piezoelectric resonances). This could be interpreted by a broad distribution of relaxations as *e.g.* in the case of another disordered material BZN [30]. In the THz range the losses are temperature independent and proportional to the frequency, which speaks in favour of a disorder induced absorption of acoustic branches (proportional to the one-phonon density of states) [31]. For $\boldsymbol{E}\perp\boldsymbol{c}$, in the IC phase, the loss spectra show again a constant background below 0.1 GHz with a temperature dependent low-frequency limit. Above 570 K no HF data are available and moreover the sample conductivity prevents reliable loss measurements.

The temperature dependence of the IR mode frequencies is depicted in Figure 8. Figure 8a shows the modes of A_1 symmetry active in the $\boldsymbol{E} \parallel \boldsymbol{c}$ polarized spectra. For comparison we added to this figure the soft Raman mode and the central mode [12], another Raman mode of higher frequency [32] and the soft mode detected in neutron

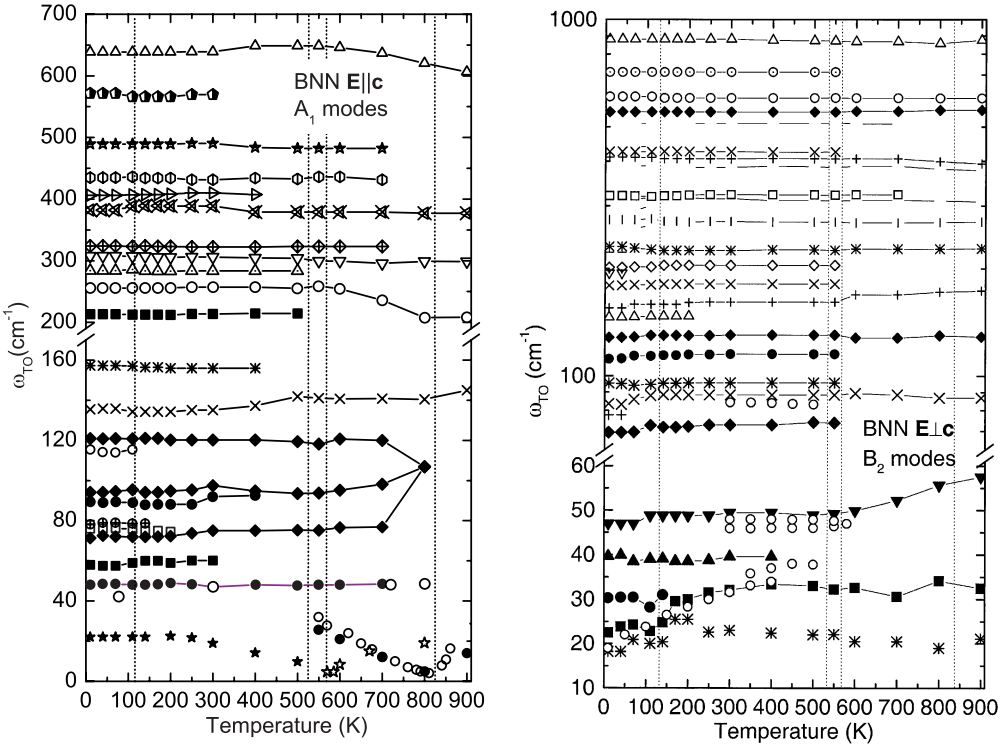

Fig. 8. Temperature dependence of the frequencies of the phonons for the $\boldsymbol{E} \parallel \boldsymbol{c}$ and $\boldsymbol{E} \perp \boldsymbol{c}$ polarizations.

scattering above the IC-ferroelastic phase [4]. Below T_c the overdamped ferroelectric soft mode is seen. We have depicted its relaxational frequency, calculated as $\omega_{TO}^2/\gamma_{TO}$. The IR frequency values are in good agreement with the Raman data around T_c [12]. Another mode of constant frequency around 50 cm^{-1} was added in agreement with a weak mode seen in Raman spectra [32]. This mode appears below T_c and should be of A_1 symmetry (both Raman and IR active). In our IR spectra it is very weak and is not directly seen. Below T_i the polar amplitudon due to the IC modulation should appear. The corresponding IR excitation is overdamped down to 250 K and in Figure 8a its relaxation frequency is shown. Below this temperature it becomes underdamped. Its frequency hardens on cooling from 500 K to RT and then saturates, in agreement with the behaviour of the order parameter of the modulation, which becomes already saturated at RT [4,33].

Figure 8b shows modes of E and both B_1-B_2 symmetry (symmetries valid in ferroelectric and ferroelastic phases, respectively) active in the $\boldsymbol{E} \perp \boldsymbol{c}$ polarized spectra. The lowest mode denoted by stars is of the central-mode type. Low-frequency Raman modes from the literature [13,14] are also included (open circles). The Raman soft mode is in very good agreement with the IR one around RT, but on lowering the temperature, near 150 K, there is a crossing between the IR soft and central mode, which prevents precise evaluation of the mode frequencies. Coupling between the central and soft mode is well known in ferroelectric materials [34] and in BNN it seems that the presence of the PT at T_0 affects the dynamics of the two modes. We have to note that there appears a shoulder in the permittivity near 150 K (see Fig. 6b), which could be expected from the coupling or the reported PT shifted to a higher temperature.

5 Conclusions

We have shown that the use of combined techniques to measure the dielectric spectrum from 10^2 to 10^{14} Hz is helpful to understand better the phonon dynamics and dielectric response of BNN crystals around all the known PTs.

The strong dielectric anomaly at $T_c = 830$ K has been satisfactorily explained by a relaxational ferroelectric soft mode coupled with a central mode. Both these relaxational modes gradually disappear in the ferroelectric phase so that this PT appears to be of order-disorder nature.

Below the incommensurate PT at T_i the use of combined Raman and neutron scattering data together with our dielectric data enabled us to estimate the frequencies of the IR amplitudon.

An incipient ferroelectric-ferroelastic PT is revealed, which explains both the increase of the permittivity $\varepsilon'_{\perp c}$ on cooling and the presence of a B_2-symmetry soft mode. In the hypothetical phase a new component of P_s should appear along the b-axis.

The transition at $T_0 = 110$ K was not revealed in our measurements, but the behaviour of the IR phonons and the LF permittivity seem to suggest that our sample shows some anomalies at slightly higher temperatures around 150 K.

The authors thank J. Hlinka for helpful discussions and J. Fabry for determining the site symmetries of the atoms. The work was supported by the Grant Agency of the Czech Republic (project No. 202/01/0612), and by the Academy of Sciences of the Czech Republic (projects No A1010213 and AVOZ1-010-914).

References

1. S. Singh, D.A. Draegert, J.E. Geusic, Phys. Rev. B **2**, 2709 (1970)
2. P.B. Jamieson, S.C. Abrahams, J.L. Bernstein, J. Chem. Phys. **50**, 4352 (1969)
3. S. Mori, N. Yamamoto, Y. Koyama, Y. Uesu, Phys. Rev. B **52**, 6158 (1995)
4. J. Schneck, J.C. Toledano, C. Joffrin, J. Aubree, B. Joukoff, A. Gabelotaud, Phys. Rev. B **25**, 1766 (1982)
5. C. Manolikas, Phys. Status Solidi (a) **68**, 653 (1981)
6. M. Verwerft, G. Van Tendeloo, J. Van Landuyet, S. Amelinckx, Ferroelectrics **88**, 27 (1988)
7. K. Fujishiro, Y. Uesu, J. Phys. Cond. Matt. **8**, 6435 (1996)
8. S. Mori, N. Yamamoto, Y. Koyama, Y. Uesu, Phys. Rev. B **55**, 11212 (1996)
9. J. Schneck, B. Joukoff, R. Mellet, Ferroelectrics **26**, 775 (1980)
10. M. Zhang, T. Yagi, W.F. Oliver, J.F. Scott, Phys. Rev. B **33**, 1381 (1986)
11. W.F. Oliver, J.F. Scott, Ferroelectrics **117**, 63 (1991)
12. G. Errandonea, H. Savary, J. Schneck, Ferroelectrics **55**, 19 (1984)
13. A. Boudou, J. Sapriel, Phys. Rev. B **21**, 61 (1980)
14. A. Shawabkeh, J.F. Scott, Phys. Rev. B **43**, 10999 (1991)
15. T. Yamada, H. Iwasaki, N. Niizeki, J. Appl. Phys. **41**, 4141 (1970)
16. A.V. Turik, E.N. Sidorenko, V.G. Kryshtop, Sov. Phys. Solid State **25**, 1177 (1983)
17. S.D. Ross, J. Phys. C **3**, 1785 (1970)
18. A. Lurio, J. Appl. Phys. **43**, 3753 (1972)
19. E. Buixaderas, S. Kamba, J. Petzelt, M. Wada, S. Ando, Ferroelectrics **239**, 17 (2000)
20. V.M. Petrov, *Dielectric measurements of Ferroelectrics* (Moscow, 1972) (in Russian)
21. J. Grigas, *Microwave Dielectric Spectroscopy of Ferroelectrics and Related Materials* (Gordon and Breach, Amsterdam, 1996)
22. P. Kužel, J. Petzelt, Ferroelectrics **239**, 79 (2000)
23. F. Gervais, *Infrared and millimeter waves*, 8, Chapter 7, 279, edited by K.J. Button (Ac. Press, New York, 1983)
24. G. Burns J.D. Axe, D.F. O'Kane, Solid State Comm. **7**, 933 (1969)
25. J.C. Toledano Phys. Rev. B **12**, 943 (1975)
26. A.W. Warner, G.A. Coquin, J.L. Fink, J. Appl. Phys. **40**, 4353 (1969)
27. J.F. Nye, *Physical properties of crystals* (Oxford, 1957)
28. W.F. Oliver, J.F. Scott, S.A Lee, S.M. Lindsay, J. Phys. Cond. Matt. **2**, 2465 (1990)
29. V. Janovec, V. Dvořák, J. Petzelt, Czech J. Phys. B **25** 1362 (1975)
30. S. Kamba, V. Porokhonskyy, A. Pashkin, V. Bovtun, J. Petzelt, J.C. Nino, S. Trolier-McKinstry, M.T. Lanagan, C.A. Randall, Phys. Rev. B **66**, 54106 (2002)
31. J. Petzelt, N. Setter, Ferroelectrics **150**, 89 (1993)
32. L.C. Bobb, J. Dahl, I. Lefkowitz, L. Muldawer, Ferroelectrics **1**, 247 (1970)
33. G. Errandonea, M. Hebbache, F. Bonnouvrier, Phys. Rev. B **32**, 1961 (1985)
34. J. Petzelt, G.V. Kozlov, A.A. Volkov, Ferroelectrics **73**, 101 (1987)